Investigating the effect of current density in ultra-fast electrolytic zinc phosphate deposition

Federico Lissandrello [a], Nora Lecis [b], Luca Magagnin [a,*]

[a] *Dipartimento di Chimica, Materiali e Ingegneria Chimica "Giulio Natta", Politecnico di Milano, Via Mancinelli, 7, Milano 20131, Italy*
[b] *Dipartimento di Meccanica, Politecnico di Milano, Via Giuseppe La Masa 1, Milano 20156, Italy*

ARTICLE INFO

ABSTRACT

The influence of the current density utilized during electrolytic zinc phosphate deposition on the properties of the final coatings has been investigated. The adoption of a concentrated electrolyte allows satisfactory coating properties with current densities as high as 100 mA cm^{-2}, resulting in exceptional deposition rates. The size of the Zn_3PO_4 crystals was shown to decrease with the current density, which in turn affected the coatings final properties. An explanation to this finding was provided following classical nucleation theory. Samples obtained at 25 and 50 mA cm^{-2} featured more compact layers while samples obtained at 100 mA cm^{-2} were thicker but porous. Scratch test was used to assess wear resistance, which was observed to be increasing with the applied current density. The more compact layers obtained at 25 and 50 mA cm^{-2} provided an enhanced corrosion resistance as highlighted by potentiodynamic polarization and electrochemical impedance spectroscopy. The adoption of an electrolytic setup allowed for co-deposition of metallic Zn which can further protect the steel substrate by galvanic coupling.

1. Introduction

Despite being among the oldest and most common surface treatments for steel, zinc phosphate coatings have recently been scrutinized due to the high energy consumption and environmental burden of the process [1,2]. Considering the ubiquitous presence of this technology in different industrial sectors, finding a more sustainable alternative is a task of paramount importance. Phosphate conversion coatings have indeed cemented themselves in a wide variety of applications, such as barriers against corrosion [3–5], lubricant carriers in preparation of cold-deformation processes [6,7] and as pretreatments before painting operations [8].

In the traditional embodiment of the process, the metallic substrate is converted into a layer of insoluble phosphates by an immersion in an acidic electrolyte containing all the necessary precursors for the film formation [9–11]. One of the main consequences of the coating process is the buildup of the byproducts of the conversion reactions, such as Fe^{2+} ions, in the electrolyte. Eventually, a sludge composed mainly of $FePO_4$ forms inside the tank which must be periodically filtered and separated, an operation that requires large quantities of energy and water [1, 12–14]. On top of this, the most common operating temperatures for

phosphating formulations lie between 65 and 85 °C, which further intensify the energetic demand of this technology [15,16].

In recent years, several alternatives to traditional phosphating have been proposed in literature, including conversion coatings based on zirconium [17–19], titanium [19–21], and vanadium [22]. However, given the exceptional versatility of phosphate coatings, it still remains unclear whether their niche can be completely filled with one of these novel formulations. In contrast, electrolytic phosphating offers a diametrically opposite solution, with the possibility of maintaining similar coating chemistry as traditional phosphating, while also preventing the formation of the sludge byproduct during the deposition [23]. This feature would allow the replacement of conversion phosphating with the electrolytic treatment in already existing supply chains with minimal disruption. The fundamental idea behind electrolytic phosphating is the application of a cathodic polarization to the steel substrate in order to promote the hydrogen evolution and nitrate reduction reactions, without having to rely on Fe dissolution [10,11]:

$$2H^+ + 2e^- \rightarrow H_2 \tag{1}$$

$$NO_3^- + 4H^+ + 3e^- \rightarrow NO + 2H_2O \tag{2}$$

As a consequence of reactions (1) and (2), a pH gradient forms at the

---

* Corresponding author.
E-mail address: luca.magagnin@polimi.it (L. Magagnin).

substrate-electrolyte interface, altering the equilibrium of phosphate species in close proximity of the steel surface. In response to the pH change, H_3PO_4 will undergo deprotonation according to the following reactions:

$$H_3PO_4 \rightarrow H_2PO_4^- + H^+ \qquad (3a)$$

$$H_2PO_4^- \rightarrow HPO_4^{2-} + H^+ \qquad (3b)$$

$$HPO_4^{2-} \rightarrow PO_4^{3-} + H^+ \qquad (3c)$$

which have respectively a pKa of 2.14, 7.21 and 12.34 [24]. Eventually this leads to the supersaturation of the poorly soluble tertiary phosphates, which precipitate on the steel surface, resulting in the formation of the film. For example, in the case of zinc phosphating:

$$3Zn^{2+} + 2PO_4^{3-} \rightarrow Zn_3(PO_4)_2 \qquad (4)$$

As it can be seen from the chemical reactions, no Fe^{2+} buildup is expected to take place in electrolytic phosphating, especially considering that a cathodic polarization would prevent iron dissolution in the first place. It is also worth noting that with the electrolytic setup it is possible to obtain satisfactory coating quality without the need of high temperatures [25–27]. Indeed, in the conversion process the deposition rate is dictated purely by a chemical equilibrium between the metal dissolution and the phosphate precipitation which could be accelerated by an increase in temperature. In contrast, the deposition rate in the electrolytic setup can be adjusted at the user discretion, simply by selecting an appropriate current density. By capitalizing on this important difference, in the study we demonstrate the possibility of obtaining exceptionally high deposition rates in electrolytic phosphating with an optimized electrolyte. In general, a high deposition rate is desirable not only for a purely improved throughput of the process, but also to minimize the risk of hydrogen embrittlement, which is thought to be one of the main drawbacks of the electrolytic process [25]. The electrolyte presented in this study was designed with a few core principles in mind:

- The initial pH of the electrolyte was chosen to be reasonably close to the pH at which $Zn_3(PO_4)_2$ would spontaneously precipitate in solution.
- A high concentration of H_3PO_4 and Zn^{2+} was employed, so that the coating formation would not be hindered by the availability of reacting species. This allowed the bath to operate at higher current densities without loss of performance.
- A rather low electrolyte pH was considered to be beneficial, in order to promote reactions (1) and (2). Similarly, a high concentration of NO_3^- was also employed.

In this study we will demonstrate how following these simple points, the deposition rate could be optimized to an almost stoichiometric regime. Moreover, we will highlight the effects of the cathodic current density, not only on the deposition rate, but also on the morphology, composition, and final properties of the coatings.

2. Materials and methods

2.1. Samples preparation

Coatings were deposited on S235 steel samples with the composition reported in Table 1 and an exposed area of 7.5 cm^2. Prior to the deposition, substrates were mechanically polished using SiC abrasive paper with 240, 320, 600 and 1200 grit. Then, samples were sonicated in

ethanol for 10 min to remove any residue of the polishing step as well as possible organic contamination of the surface. After drying, the substrates were pickled in a 10 wt.% H_2SO_4 for 1 min and rinsed with deionized water. Finally, the surface of the samples was activated by immersion in a 3 g/l colloidal titanium phosphate solution (JUBOfine 1000, JUBO Technologies GmbH) for 30 s. The use of an activator is a well-documented procedure for conversion phosphating [28,29] and while it's not strictly necessary for the formation of the coatings, it provides exceptional improvements in their quality. Briefly, the titanium phosphate colloidal particles adhere to the surface of the steel and act as nucleation sites for zinc phosphate, increasing the nucleation rate and leading to a finer crystalline structure.

2.2. Zinc phosphate coating deposition

All the reagents used in the electrolyte formulation were purchased from Sigma-Aldrich. The composition of the electrolyte used for all the depositions in this study is shown in Table 2. ZnO, H_3PO_4 and HNO_3 were used as precursors for the electrolyte, while NaOH was used to adjust the initial pH. For this electrolyte, it was observed that at 40 °C spontaneous $Zn_3(PO_4)_2$ precipitation would take place if the pH was raised above 1.7. Following the criteria highlighted in the introduction, we adjusted the initial pH to be 1.4 for all the depositions, slightly below the pH of spontaneous precipitation.

The depositions were carried out at 40 °C under mild stirring in a two-electrode electrochemical cell with the steel samples as the working electrode and a Ti-MMO mesh as the counter electrode. For three-electrode depositions, an Ag/AgCl (3 M KCl) was introduced as the reference electrode. After the deposition, the samples were rinsed with abundant deionized water and dried under a N_2 stream.

2.3. Coating characterization

X-ray diffraction (XRD) measurements were performed using a Philips PW1830 diffractometer equipped with a Cu source ($K_{\alpha 1}Cu = 1.54058$ Å). A Zeiss EVO 50 EP scanning electron microscope (SEM) coupled with an energy dispersive X-ray analyzer (EDS) Model 7060 from Oxford Instruments were used to investigate the coatings morphology and composition. Scratch test was carried out with a MCTX S/N 50–0223 from CSM instruments equipped with a Rockwell indenter and a 200 μm spherical diamond tip. For the tests, the load was varied linearly from 0.3 to 30 N at a rate of 10 N min^{-1}, while the total length of the scratch was 5 mm. Corrosion tests were performed in Na_2SO_4 0.1 M in a three-electrode configuration with an Ag/AgCl (3 M KCl) and a platinum mesh as the reference and counter electrodes respectively. First, the open circuit potential (OCP) was measured for 60 min, then potentiodynamic polarization tests were carried out starting from -250 mV vs OCP with a scan rate of 1 mV s^{-1} up to $+200$ mV vs Ag/AgCl. Additionally, electrochemical impedance spectroscopy (EIS) measurements were also collected using a sinusoidal perturbation with a 10 mV amplitude and a frequency ranging from 10^5 to 10^{-1} Hz. Prior to EIS measurements, the OCP was also measured for 60 min. Corrosion measurements were repeated twice to ensure repeatability of the results.

Table 2
Composition of the electrolyte used for phosphate coating deposition.

Zn^{2+}	PO_4^{3-}	NO_3^-	NaOH
45 g/l	75 g/l	68 g/l	Until pH = 1.4

Table 1
Composition of the S235 steel substrates.

Element	C	Mn	P	S	Si	Al	Ni	Cr	Cu	Fe
%	0.075	0.460	0.015	0.010	0.020	0.040	0.015	0.015	0.010	Balance

3. Results and discussion

Zinc phosphate coatings were obtained by galvanostatic deposition at 25, 50 and 100 mA cm^{-2}, while the total charge density was varied between 0.6 and 3.0 C cm^{-2} by properly adjusting the deposition times. For each condition, the coating weight of three different samples was measured. Typically, the measurement of coating weight in conversion phosphating is obtained by the difference in the mass of the sample before and after a dissolution step, which completely removes the coating, while leaving the substrate unaffected [30]. This is done to prevent severe underestimation of the coating weight due to the concurring substrate dissolution taking place during coating formation. However, considering the nature of the electrolytic process, we deemed this step to be unnecessary, thus the coating weight of the samples was measured by simply taking the difference in mass before and after the deposition and dividing it by the exposed area. The results in Fig. 1a show a linear relationship between the coating weight and the deposition time for all the tested current densities. In all the cases, the maximum coating weight was around 30 g m^{-2} and was obtained with deposition times between 30 and 120 s. Interestingly, when the coating weight is plotted as a function of the charge density (Fig. 1b), all the points seem to follow the same linear relationship, regardless of the current density used. At first glance, this might not appear surprising at all, since Faraday's law of electrolysis already states that the amount of species reacting at the electrode is directly proportional to the electrical charge passing through it. However, in the case of zinc phosphate precipitation a transfer of electrons is involved only in reactions (1) and (2) which are responsible for the consumption of H$^+$ ions at the interface, setting up the proper conditions for reaction (4) to take place. Once the pH conditions are met, zinc phosphate precipitation will take place as long as there is a steady supply of Zn^{2+} and PO$_4^{3-}$ ions. By adopting a concentrated electrolyte, it's possible to ensure that reaction (4) will never be limited by mass transfer limitations, but only by the amount of phosphate ions generated by the deprotonation of phosphoric acid, which in turn is related to the amount of H$^+$ consumed by reactions (1) and (2). In fact, in these conditions it could be possible to provide a first order approximation of the expected deposited mass if we consider the stoichiometry of the reactions involved (details in supporting information). For a reduction process purely driven by nitrate reduction, a charge density of 3.0 C cm^{-2} would lead to a coating weight of 31.7 g m^{-2}, which is substantially close to the average coating weight measured in this study (29.9 g m^{-2}). To make a counterexample: if the rate of phosphate growth was independent from the applied current density, a decrease in the coating weight should be observed as the current density is increased, purely because of the reduced deposition times. The direct proportionality between electric charge and coating weight instead suggests that the whole deposition process is determined by the electron transfer reactions. This condition cannot be assumed *a priori* and will most likely not hold true for different deposition parameters and electrolyte formulations. Furthermore, we believe that this condition is necessary to achieve satisfactory coating quality, since an excessive consumption of H$^+$ ions would lead to the migration of the pH gradient away from the surface, resulting in the formation of loosely attached phosphate crystals [13,16,31].

Overall, the results presented in Fig. 1a and 1b point out the benefits of adopting a well-optimized electrolyte for electrolytic phosphate coating: to put the numbers presented in this study in perspective, other works on electrolytic zinc phosphating report similar coating weights with deposition times ranging from 5 to 30 min, which is a consequence of the low current used in those cases [13,26,32]. Even when normalized with respect to electric charge, a deposition rate of 0.98 mg C^{-1} is 2 to 3 times higher than the ideal conditions presented in other studies.
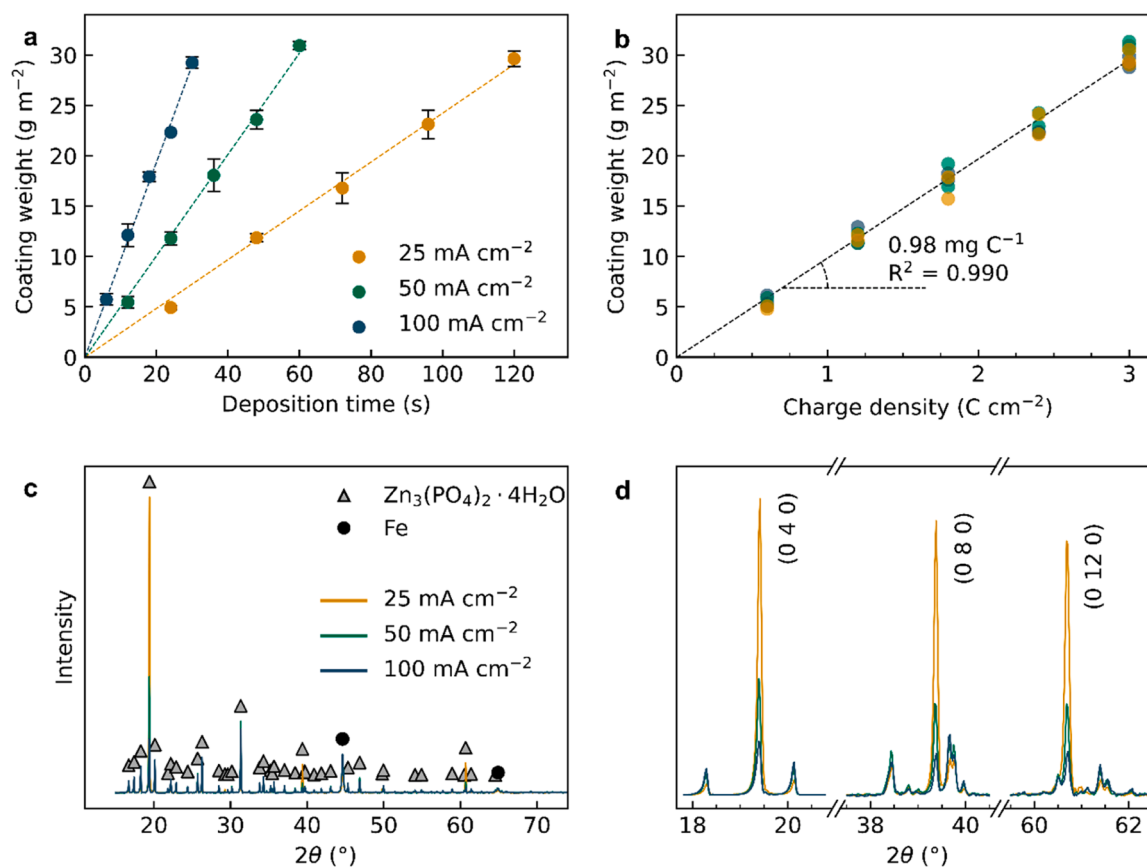

Fig. 1. Coating weight of zinc phosphate obtained at 25, 50 and 100 mA cm^{-2} as a function of (a) deposition time and (b) charge density. (c) XRD diffractogram of zinc phosphate coatings. (d) Close-up of peaks belonging to the (0 4n 0) direction, with n = 1, 2 and 3.

Considering the results presented so far, all the samples for the successive tests were produced with a charge density of 3.0 C cm^{-2} unless otherwise specified.

The results of XRD analysis of the zinc phosphate coatings (Fig. 1c) showed peaks of crystalline $Zn_3(PO_4)_2 \bullet 4H_2O$ (ICSD: 413638), also known as hopeite [33], as well as peaks associated to metallic Fe from the substrate (ICSD: 14754). Interestingly, it appears that deposition at lower current densities leads to a preferential orientation of growth along directions (0 4n 0), as highlighted by the increased intensity of their correlated peaks at 19.4°, 39.4° and 60.7° (Fig. 1d). As expected, there was no signal that could be attributed to a $Zn_2Fe(PO_4)_2$ phase, which is typically formed in conversion phosphating due to the buildup of Fe^{2+} ions in solution [30]. The absence of $Zn_2Fe(PO_4)_2$, also known as phosphophyllite, reflects the different initiation mechanism for phosphate precipitation in electrolytic phosphating: despite featuring an electrolyte with lower pH than common conversion phosphating formulations, the electrolytic process completely prevents the dissolution of the substrate thanks to the cathodic polarization maintained during the deposition.

The SEM images in Fig. 2a–c highlight the changes in the surface morphology as a function of the current density. As it can be seen, an increase in the deposition current led to a significant reduction of the average crystal size, which is in line with other studies on electrolytic phosphate coating [34–36]. Classical nucleation theory [37–39] provides a good foundation to explain the origin of these findings: the nucleation rate (J), i.e. the number of nucleation events taking place on the surface per unit time, can be expressed as the product of two exponentials, which are respectively related to the kinetics and thermodynamic of the event:

$$J = A \cdot e^{-\frac{E_A}{k_B T}} \cdot e^{-\frac{\Delta G_N}{k_B T}} \tag{5}$$

where E_A and ΔG_N are respectively the kinetic activation energy and the difference in free energy for a single nucleation event, while k_B is Boltzmann's constant, T is the absolute temperature, and A is a pre-exponential factor. Generally, the kinetic term is often neglected because its quantification is a challenging task [38]. On the other hand,
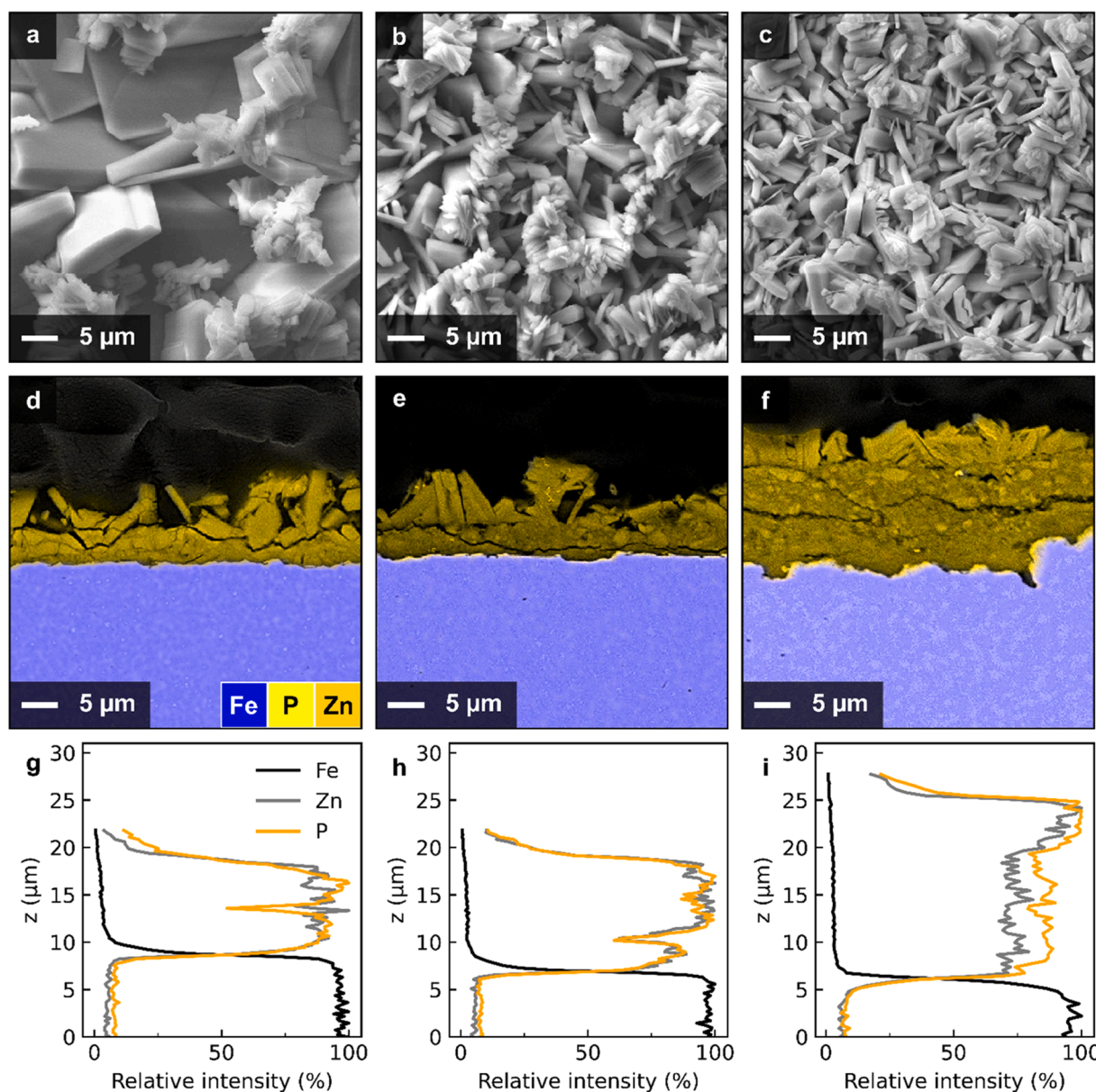

Fig. 2. (a–c) SEM images of the zinc phosphate coatings obtained at 25, 50 and 100 mA cm^{-2}. (d-f) EDS mapping of the coatings cross-section. (g-i) Integration of the EDS signal of Zn, P and Fe along the vertical direction.

the thermodynamic barrier for nucleation can be expressed as:

$$\Delta G_N = \alpha \frac{\gamma^3}{\Delta\mu^2} \tag{6}$$

where α is a geometrical factor, $\Delta\mu$ is the change in chemical potential of the crystallizing species, and γ is the interfacial free energy, that is, the surface contribution to free energy per unit area of the growing nuclei. In the case of homogeneous nucleation, γ is a constant of the material that composes the new phase that is being formed. This constant should be adjusted in the instance of heterogeneous nucleation [40], such as the formation of zinc phosphate nuclei on an activated steel surface, but does not depend on the electrolyte composition. Accordingly, for the purposes of this study we can assume α and γ fluctuations to be negligible across the different samples. This leaves $\Delta\mu$ to be the only variable affected by the current density. Indeed, $\Delta\mu$ can be expressed in terms of the supersaturation of the solution (S) according to [39,41,42]:

$$\Delta\mu = k_B T \ln(S) = k_B T \ln\left(\frac{A_P}{K_{SP}}\right) \tag{7}$$

with A_P and K_{SP} being respectively the activity product and the solubility product of the nucleating phase. Finally, by combining Eqs. (5), (6) and (7) it's possible to express the dependence of the nucleation rate with the supersaturation [42,43]:

$$J \approx \exp\left(-\frac{1}{(\ln(S))^2}\right) \tag{8}$$

The conditions for phosphate precipitation require $S > 1$, resulting in $J(S)$ being a monotonically increasing function in this range. As the supersaturation at the interface increases, a finer crystal structure should be expected. In other words, it can be assumed that the changes in morphology shown in Fig. 2a-c originate strictly from the relationship between current density and nucleation rate.

From EDS analysis of the coatings cross-section in Fig. 2d–f, it appears that the current density also affected the thickness of the films. In particular, the average thickness of the sample obtained at 100 mA cm^{-2} (17.94 μm) was more than double than the thickness of the samples obtained at 25 mA cm^{-2} (7.61 μm) and 50 mA cm^{-2} (7.16 μm). This result is quite peculiar when considering that the samples have a comparable coating weight, suggesting a prominently increased porosity when high current densities were employed. This difference could be attributed to the increased hydrogen evolution rate: when the gas bubbles are not properly evacuated from the surface, they interfere with the coating growth, essentially forming a barrier between the substrate and the electrolyte. The signal from the EDS probe was also integrated along the thickness of the samples (Fig. 2g–i) in order to gauge any composition gradient in the coating. In fact, one of the main features of electrolytic zinc phosphating is the direct electroplating of metallic zinc from the Zn^{2+} ions in solution. According to Jegannathan et al. [25,44], a thin layer of metallic Zn is formed on the surface of the steel before Zn$_3$(PO$_4$)$_2$ precipitation can take place; however we observed that the signals of Zn and P in Fig. 2g–i follow similar trends along the vertical direction, suggesting a homogeneous composition of the film. Still, EDS measurements of the surface chemical composition reveal a Zn/P ratio of 1.55, 1.55 and 1.50 for samples deposited at 25, 50 and 100 mA cm^{-2} respectively. Considering that the stoichiometric ratio of a pure hopeite coating would be 1.5, any excess in the Zn/P ratio is attributed to the presence of metallic Zn. Perhaps the high current densities adopted in this study do not allow the formation of a complete film of zinc at the base of the coating. Indeed, in a previous work by Kellner et al. [45] where high current densities were also employed, it was shown that zinc was preferentially deposited in small channels protruding from the steel surface.

In order to gain insights on the coating formation mechanism, additional depositions in a three-electrode cell with an Ag/AgCl (KCl 3

M) reference electrode were carried out. The time evolution of the potential of the working electrode for the different current densities is shown in Fig. 3a: the three curves showed a sudden potential drop in the first seconds of deposition followed by a small nucleation peak, similar to what is observed during zinc electrodeposition [46–48]. The potential then slowly decreased until a plateau was reached and did not change significantly for the rest of the deposition. In general, it appears that irrespective of the current utilized during the deposition, the potential evolution retains consistent features, although curves obtained with lower currents are dilated on the time axis and feature higher potential plateaus, due to the reduced reaction rate and lower polarization of the electrode.

The evolution of the surface morphology was monitored by preparing samples at 50 mA cm^{-2} and stopping the deposition after 2.5, 10, 20 and 60 s. The SEM image in Fig. 3b revealed the initiation of Zn$_3$(PO$_4$)$_2$ nucleation just 2.5 s into the process, showcasing the possibility of reducing the initiation time to achieve zinc phosphate precipitation, possibly thanks to the small pH gap required by the concentrated electrolyte [49]. Between 2.5 s and 10 s, the potential decreased rapidly while the zinc phosphate crystals grew, covering a larger portion of the steel surface (Fig. 3c). Although a certain degree of polarization is expected during the first seconds of deposition because of the formation of concentration gradients at the interface, it's also worth noting that because of the poor electric conductivity of Zn$_3$(PO$_4$)$_2$, any electron transfer between the surface and the electrolyte is effectively hindered [50,51]. This self-inhibiting behavior explains why a higher polarization is required to maintain the same current density as the zinc phosphate layer develops. In practical terms, this feature proves to be advantageous as it leads to a planar growth of the coating on the steel surface before its development along the vertical direction. Indeed, after 20 s the potential reached a plateau and the related SEM image in Fig. 3d shows complete coverage of the substrate. Interestingly, at this stage a set of smaller particles with irregular shape also began to appear, located predominantly at the boundary between the already existing crystals. This morphology change could be explained by considering that the current lines would concentrate primarily on the exposed steel, effectively increasing the local current density, which would in turn lead to a finer crystalline structure according to the mechanisms explained previously. Once the potential plateau was reached, no significant changes in the morphology were observed (Fig. 3e).

The wear resistance and adhesion of the coatings on the steel substrate was assessed with scratch tests using a 200 μm diamond spherical tip. Following previous literature on scratch testing of Ca [52,53] and Ca-Zn [54] phosphate coatings, two critical loads were identified with the aid of optical microscopy, SEM as well as acoustic emission from the indenter. Specifically, the two critical loads were associated to the initial delamination (Lc1) and the total delamination of the film (Lc2).

Three scratches from representative samples presented in Fig. 4a-c highlight the different behavior of the coatings obtained at 25, 50 and 100 mA cm^{-2}. As the indenter swept across the dark phosphate crystals from left to right, the shiny gray steel substrate was exposed. With small loads the coatings failed in sporadic locations, leaving patches of exposed steel; the lowest load at which this kind of failure occurred was then considered the Lc1. Eventually, the load became high enough that the coating was entirely removed, which can be more easily noticed for the sample obtained at 25 mA cm^{-2}. The quantitative analysis of the critical loads in Fig. 4d shows that a higher current density led to an increase in both critical loads and therefore to a better wear resistance of the film. Upon closer inspection, it appeared that the larger particles were easily detached from the substrate (Fig. 4e), while the smaller ones could instead deform under the spherical indenter (Fig. 4f), forming the so-called "glaze" layer which is a typical feature of phosphate coatings [55–57]: as the phosphate crystals are crushed and compacted under the load, a lump of debris can pile-up in front of the indenter that acts as a material reservoir, leading to the formation of a compact, hard, yet brittle layer [55]. We believe that two factors played a role in
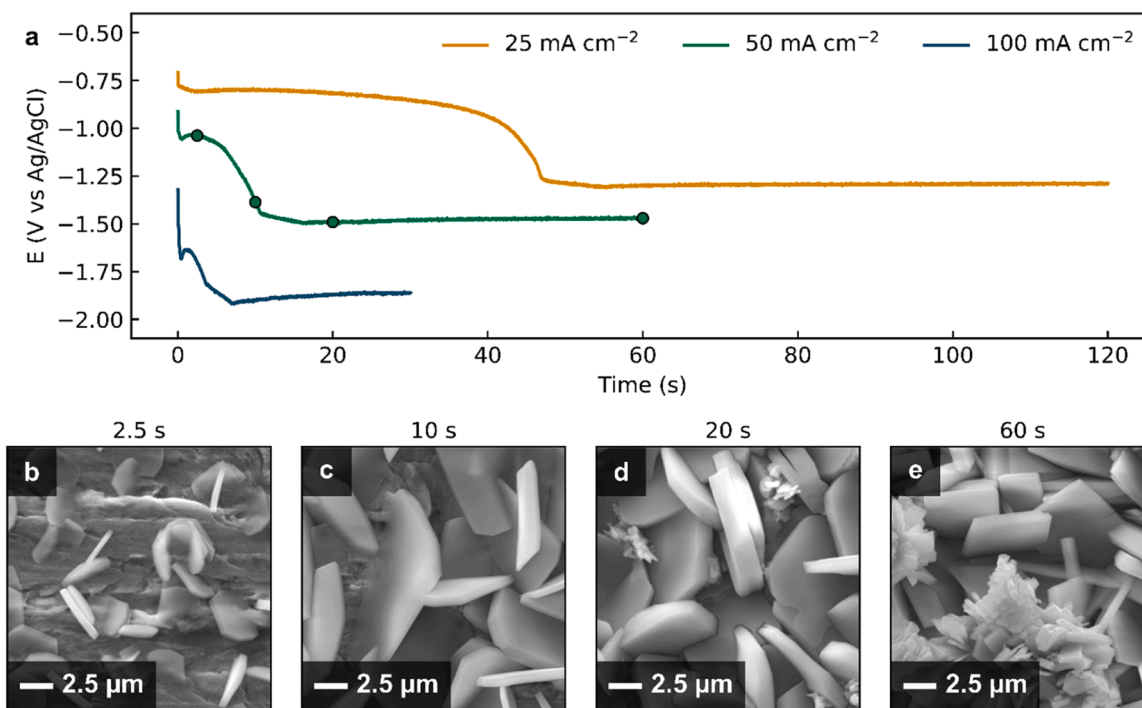
Fig. 3. (a) Potential profile for depositions with 25, 50 and 100 mA cm^{-2} in three electrode cells. Dots indicate the conditions at which SEM images (b-e) were taken.
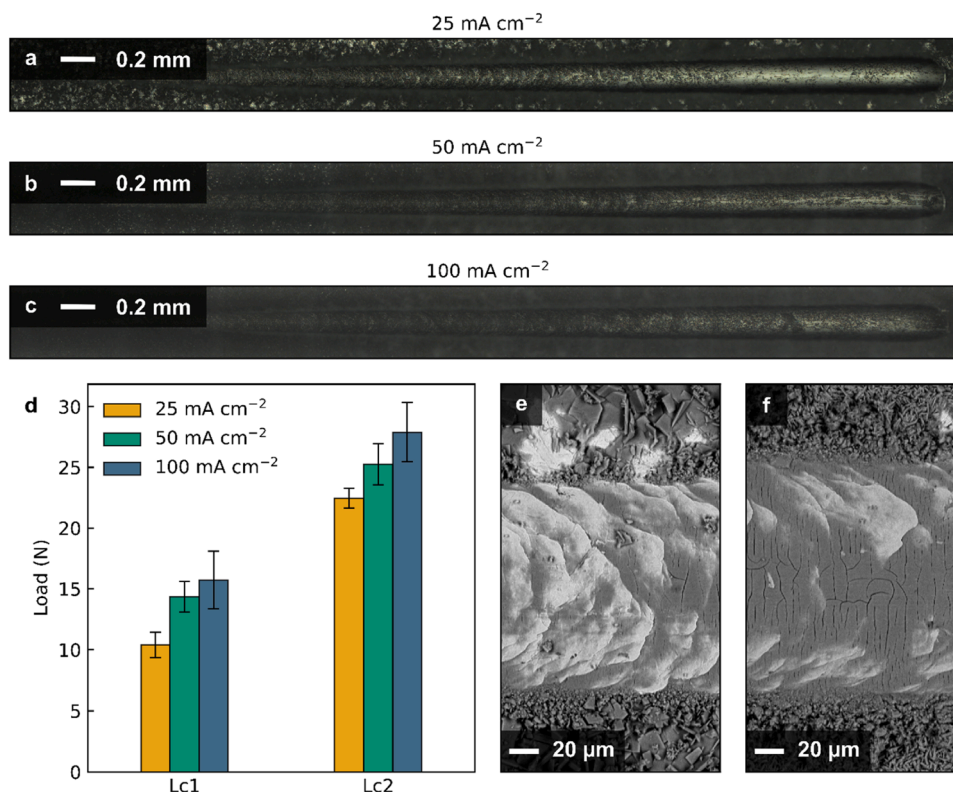

Fig. 4. (a–c) Wear tracks of the coatings obtained at 25, 50, 100 mA cm^{-2} as observed under the optical microscope. (d) Critical loads of the zinc phosphate coatings ($N = 3$). (e–f) Backscattered electrons SEM image of the wear track of the coatings obtained at 25 and 100 mA cm^{-2}.

determining the significantly higher critical loads exhibited by the coatings obtained at 100 mA cm^{-2}: first, the intrinsic porosity of the coatings produced at higher current densities would allow for an easier accommodation of the lateral expansion of the zinc phosphate crystals, thereby facilitating their deformation; furthermore, the smaller crystals obtained in these conditions are more likely to accumulate in front of the indenter, creating the lump of debris necessary for the formation of the glaze layer. On a similar note, this would also explain the different appearance of the sides (Fig. 4e-f) and the end of the wear tracks (Figures S1 and S2): while the deposit obtained at 100 mA cm^{-2}

exhibited massive lateral pile-up, the large crystals obtained at 25 mA cm^{-2} tended to flake off easily, leaving areas of exposed steel even outside of the wear track.

Finally, the corrosion resistance of the as-obtained coatings was tested in Na$_2$SO$_4$ 0.1 M and compared to the uncoated steel. The potentiodynamic polarization curves in Fig. 5a clearly denote a significant overpotential for iron dissolution as pointed out by the shift of the anodic branch between −0.7 and −0.3 V vs Ag/AgCl. This phenomenon has already been documented in the case of zinc and manganese phosphate coatings obtained with the conversion process and has been attributed to the barrier properties of the films [3,58]. As the active steel surface is covered with the inert phosphate coating, the kinetics of iron dissolution is inhibited, leading to a reduced corrosion rate. Another evident consequence of the electrolytic phosphate treatment was the shift in the corrosion potential (E$_{corr}$) towards lower values, which is attributed to the presence of metallic zinc in the deposits. In regards to corrosion behavior, the galvanic coupling between the deposited zinc and the steel ensures that the substrate will be protected even in presence of defects or open porosities, similar to the protection imparted by hot-dip galvanized steel [59,60]. This sacrificial protection is not observed in phosphate coatings obtained with the conversion method, purely because no zinc deposition can take place without the application of an external current. In conclusion, it's reasonable to expect a double protection mechanism taking place in this scenario: initially the steel is in a state of cathodic protection with metallic zinc corroding in its place; eventually, as the zinc is dissolved, the barrier effect of phosphates will take over, ensuring long-term stability. Table 3 reports the corrosion current density (j$_{corr}$), as well as the cathodic and anodic slopes (β$_c$ and β$_a$) extracted with the Tafel extrapolation method [61]. As it can be seen, electrolytic zinc phosphate coatings obtained at 25 and 50 mA cm^{-2}

Table 3
Parameters extracted from Tafel extrapolation in 0.1 M Na$_2$SO$_4$.

Sample	E$_{corr}$ (V vs Ag/AgCl)	j$_{corr}$ (μA cm^{-2})	β$_c$ (mV dec^{-1})	β$_a$ (mV dec^{-1})
Uncoated	−0.696	9.521	221.0	66.5
25	−1.010	0.424	193.0	42.2
50	−1.060	0.057	110.7	45.0
100	−0.959	5.146	429.7	56.7

proved to be extremely effective in decreasing the corrosion current density. Furthermore, the high cathodic slopes pointed out to a diffusion-limited corrosion mechanism.

The results from potentiodynamic polarization were corroborated with EIS measurements. From the Nyquist plot in Fig. 5b, it can be observed that the zinc phosphate coatings featured different electrochemical behavior according to the current density used during the deposition. Coatings obtained at 25 and 50 mA cm^{-2} exhibited a flattened semi-circle that at low frequencies terminated in a 45° line. This behavior can be associated to a semi-infinite diffusivity [62], which is typical of barrier coatings, including phosphate coatings [3,25]. The diffusion tail was completely absent in the coated sample obtained at 100 mA cm^{-2}, which instead appeared as a flattened semi-circle in the orthonormal Nyquist representation. In general, the flattening of the curves is observed in porous electrodes due to a dispersion of the time constants [4,63], which can be described accurately by theoretical models [64,65]. In fact, these models have also been successfully applied to conversion phosphate coatings [4,29,66]; however we deemed that the amount of information available on the distribution of the metallic Zn in the samples presented in this work is insufficient to allow a proper
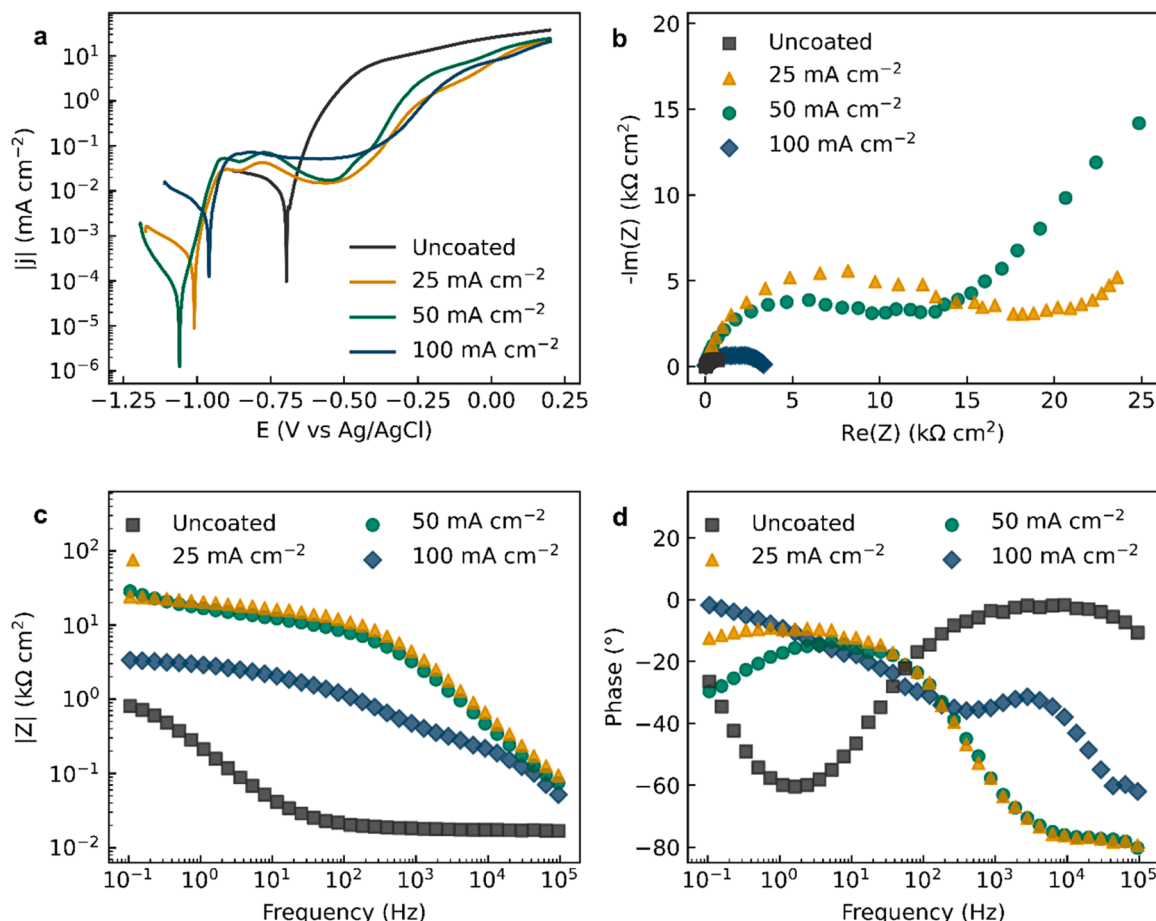

Fig. 5. (a) potentiodynamic polarization curves obtained in 0.1 Na$_2$SO$_4$. (b) Nyquist plot of the EIS results. (c, d) Bode representation of the EIS results.

description of the surface. Still, the Bode modulus plot in Fig. 5c shows that the impedance at low frequencies, often directly correlated to corrosion resistance [67,68], followed the trend $|Z|_{50} \approx |Z|_{25} > |Z|_{100} > |Z|_{uncoated}$ which is coherent with the results from the potentiodynamic polarization tests. Moreover, the same progression is observed with the phase angle at high frequencies, which is another criterion often used to evaluate the integrity of barrier coatings [69]. Briefly, a generic electrode-electrolyte interface can be modeled after a resistor in parallel with a capacitor; in this scenario, an ideal, defect-free barrier coating would not allow any electric charge transfer, resulting in a purely capacitive behavior, characterized by a phase angle of $-90°$. Conversely, an exposed metallic surface would exhibit minimal capacitive contribution and therefore could be approximated by a resistor with phase angle of $0°$. Any real surface will therefore feature a phase angle between these two extremes, with the best performing coatings reaching values closer to $-90°$ [69–71]. Indeed, from the Bode phase plot (Fig. 5d) it can be seen that the zinc phosphate coatings deposited at 25 and 50 mA cm^{-2} had a phase angle of $-77.1°$ and -76.7 respectively at 10^4 Hz; in contrast, the uncoated steel had a phase angle of just $-2.8°$, while the sample coated at 100 mA cm^{-2} reached only $-43.2°$. Overall, the results from the accelerated corrosion tests seem to point out the detrimental effects of the usage of an excessive current during zinc phosphate electrolytic deposition. Considering the higher E$_{corr}$, the different impedance response and the porous morphology, it is reasonable to believe that the deposition at higher current densities produces defects that extends through the entire thickness of the coating, possibly leaving the steel substrate completely exposed to a corrosion attack. In contrast, the compact layers produced at 25 and 50 mA cm^{-2} are excellent barriers against corrosion and the sacrificial nature of the co-deposited metallic Zn allows for a greater degree of protection that phosphate coatings obtained with the conversion treatment simply cannot offer.

4. Conclusions

In this work we outlined a few guidelines that can be used to design an optimized electrolyte for electrolytic zinc phosphating. The combination of high current densities and optimized electrolyte allows for an outstanding deposition rate to be obtained, while also keeping a relatively low temperature during the deposition. Ultimately, we showed that the current density does not merely dictate the deposition rate of the coating but is a fundamental parameter which can be tuned to meet the specific requirements of the final application. Deposits obtained at low current densities are more compact, making them an excellent solution for corrosion protection, especially when the co-deposition of metallic zinc is factored in. Conversely, the fine-grained morphology of the coatings obtained at high current density provides an improvement in wear resistance, while the highly porous structure makes them ideal as excellent lubricant carrier layers.

CRediT authorship contribution statement

Federico Lissandrello: Conceptualization, Data curation, Formal analysis, Investigation, Methodology, Visualization, Writing – original draft, Writing – review & editing. **Nora Lecis:** Investigation. **Luca Magagnin:** Conceptualization, Data curation, Methodology, Supervision, Validation, Writing – original draft, Writing – review & editing.

Declaration of competing interest

The authors declare that they have no known competing financial interests or personal relationships that could have appeared to influence the work reported in this paper.

Data availability

Data will be made available on request.

Supplementary materials

Supplementary material associated with this article can be found, in the online version, at doi:10.1016/j.electacta.2024.143840.

References

[1] M. Kobya, E. Demirbas, A. Dedeli, M.T. Sensoy, Treatment of rinse water from zinc phosphate coating by batch and continuous electrocoagulation processes, J. Hazard. Mater. 173 (2010) 326–334, https://doi.org/10.1016/j.jhazmat.2009.08.092.

[2] M.H. Shahini, H. Eivaz Mohammadloo, B. Ramezanzadeh, Recent advances in steel surface treatment via novel/green conversion coatings for anti-corrosion applications: a review study, J. Coat. Technol. Res. 19 (2022) 159–199, https://doi.org/10.1007/s11998-021-00466-0.

[3] D. Weng, P. Jokiel, A. Uebleis, H. Boehni, Corrosion and protection characteristics of zinc and manganese phosphate coatings, Surf. Coat. Technol. 88 (1997) 147–156, https://doi.org/10.1016/S0257-8972(96)02860-5.

[4] S. Silva-Fernández, B. Díaz, I. Feijoo, X.R. Nóvoa, C. Pérez, Influence of pH and temperature in the performance of Zn phosphate conversion coatings, Electrochim. Acta 457 (2023) 142510, https://doi.org/10.1016/j.electacta.2023.142510.

[5] B. Díaz, L. Freire, M. Mojío, X.R. Nóvoa, Effect of carbon on the corrosion and wear performance of Zn-phosphate layers, Electrochim. Acta 202 (2016) 299–309, https://doi.org/10.1016/j.electacta.2015.12.083.

[6] M. Gariety, G. Ngaile, T. Altan, Evaluation of new cold forging lubricants without zinc phosphate precoat, Int. J. Mach. Tools Manuf. 47 (2007) 673–681, https://doi.org/10.1016/j.ijmachtools.2006.04.016.

[7] P. Saffarzade, A.A. Amadeh, N. Agahi, Study of tribological and friction behavior of magnesium phosphate coating and comparison with traditional zinc phosphate coating under dry and lubricated conditions, Tribol. Int. 144 (2020) 106122, https://doi.org/10.1016/j.triboint.2019.106122.

[8] N. Rani, A.K. Singh, S. Alam, N. Bandyopadhyay, M.B. Denys, Optimization of phosphate coating properties on steel sheet for superior paint performance, J. Coat. Technol. Res. 9 (2012) 629–636, https://doi.org/10.1007/s11998-012-9395-9.

[9] E.I. Ghali, R.J.A. Potvin, The mechanism of phosphating of steel, Corros. Sci. 12 (1972) 583–594, https://doi.org/10.1016/S0010-938X(72)90118-7.

[10] D. Zimmermann, A.G. Muñoz, J.W. Schultze, Microscopic local elements in the phosphating process, Electrochim. Acta 48 (2003) 3267–3277, https://doi.org/10.1016/S0013-4686(03)00385-2.

[11] L. Kouisni, M. Azzi, M. Zertoubi, F. Dalard, S. Maximovitch, Phosphate coatings on magnesium alloy AM60 part 1: study of the formation and the growth of zinc phosphate films, Surf. Coat. Technol. 185 (2004) 58–67, https://doi.org/10.1016/J.SURFCOAT.2003.10.061.

[12] Y.M. Kuo, An alternative approach to recovering valuable metals from zinc phosphating sludge, J. Hazard. Mater. 201–202 (2012) 265–272, https://doi.org/10.1016/J.JHAZMAT.2011.11.081.

[13] C. Kavitha, T.S.N. Sankara Narayanan, K. Ravichandran, M.H. Lee, Deposition of zinc-zinc phosphate composite coatings on aluminium by cathodic electrochemical treatment, Surf. Coat. Technol. 258 (2014) 539–548, https://doi.org/10.1016/j.surfcoat.2014.08.040.

[14] M. Sienkowski, M. Petschel, Reduction of Sludge in a Zinc Phosphating Process - A DOE Study, SAE Trans. 106 (1997) 755–764. http://www.jstor.org/stable/44657619.

[15] F. Fang, J. Jiang, S.Y. Tan, A. Ma, J. Jiang, Characteristics of a fast low-temperature zinc phosphating coating accelerated by an ECO-friendly hydroxylamine sulfate, Surf. Coat. Technol. 204 (2010) 2381–2385, https://doi.org/10.1016/j.surfcoat.2010.01.005.

[16] K. Ravichandran, T.S.N. Sankara Narayanan, Studies on acceleration of the low temperature zinc phosphating processes, Trans. Inst. Met. Finish. 79 (2001) 143–145, https://doi.org/10.1080/00202967.2001.11871383.

[17] A. Ghanbari, M.M. Attar, Surface free energy characterization and adhesion performance of mild steel treated based on zirconium conversion coating: a comparative study, Surf. Coat. Technol. 246 (2014) 26–33, https://doi.org/10.1016/j.surfcoat.2014.02.057.

[18] H.R. Asemani, P. Ahmadi, A.A. Sarabi, H.Eivaz Mohammadloo, Effect of zirconium conversion coating: adhesion and anti-corrosion properties of epoxy organic coating containing zinc aluminum polyphosphate (ZAPP) pigment on carbon mild steel, Prog. Org. Coatings 94 (2016) 18–27, https://doi.org/10.1016/J.PORGCOAT.2016.01.015.

[19] I. Milošev, G.S. Frankel, Review—conversion coatings based on zirconium and/or titanium, J. Electrochem. Soc. 165 (2018) C127–C144, https://doi.org/10.1149/2.0371803jes.

[20] A. Abrashov, N. Grigoryan, T. Vagramyan, N. Asnis, On the mechanism of formation of conversion titanium-containing coatings, Coatings 10 (2020) 328, https://doi.org/10.3390/COATINGS10040328. Page10 (2020) 328.

[21] H. Eivaz Mohammadloo, A.A. Sarabi, Ti-based conversion coatings on cold-rolled steel substrate: the effect of practical parameters and Ti source on surface and

electrochemical properties, Corrosion 72 (2016) 791–804, https://doi.org/10.5006/1936.

[22] M. Motamedi, M.M. Attar, Nanostructured vanadium-based conversion treatment of mild steel substrate: formation process: via noise measurement, surface analysis and anti-corrosion behavior, RSC Adv. 6 (2016) 44732–44741, https://doi.org/10.1039/c6ra06064a.

[23] S. Jegannathan, T.S.N. Sankara Narayanan, K. Ravichandran, S. Rajeswari, Formation of zinc-zinc phosphate composite coatings by cathodic electrochemical treatment, Surf. Coat. Technol. 200 (2006) 4117–4126, https://doi.org/10.1016/j.surfcoat.2005.04.022.

[24] K.J. Powell, P.L. Brown, R.H. Byrne, T. Gajda, G. Hefter, S. Sjöberg, H. Wanner, Chemical speciation of environmentally significant heavy metals with inorganic ligands. Part 1: the Hg2+– Cl–, OH–, CO32–, SO42–, and PO43– aqueous systems (IUPAC technical report), Pure Appl. Chem. 77 (2005) 739–800, https://doi.org/10.1351/pac200577040739.

[25] S. Jegannathan, T.K. Arumugam, T.S.N.S. Narayanan, K. Ravichandran, Formation and characteristics of zinc phosphate coatings obtained by electrochemical treatment: cathodic vs. anodic, Prog. Org. Coat. 65 (2009) 229–236, https://doi.org/10.1016/j.porgcoat.2008.11.009.

[26] S. Jegannathan, T.S.N. Sankara Narayanan, K. Ravichandran, S. Rajeswari, Formation of zinc phosphate coating by anodic electrochemical treatment, Surf. Coat. Technol. 200 (2006) 6014–6021, https://doi.org/10.1016/j.surfcoat.2005.09.017.

[27] F. Simescu, H. Idrissi, Corrosion behaviour in alkaline medium of zinc phosphate coated steel obtained by cathodic electrochemical treatment, Corros. Sci. 51 (2009) 833–840, https://doi.org/10.1016/j.corsci.2009.01.010.

[28] P.E. Tegehall, The mechanism of chemical activation with titanium phosphate colloids in the formation of zinc phosphate conversion coatings, Colloids Surf. 49 (1990) 373–383, https://doi.org/10.1016/0166-6622(90)80118-N.

[29] B. Díaz, L. Freire, M. Mojío, X.R. Nóvoa, Optimization of conversion coatings based on zinc phosphate on high strength steels, with enhanced barrier properties, J. Electroanal. Chem. 737 (2015) 174–183, https://doi.org/10.1016/j.jelechem.2014.06.035.

[30] T.S.N.S. Narayanan, Phosphate conversion coatings - a metal pretreatment process, Corros. Rev. 12 (1994) 201–238, https://doi.org/10.1515/CORRREV.1994.12.3-4.201.

[31] W. Zai, Y. Su, H.C. Man, J. Lian, G. Li, Effect of pH value and preparation temperature on the formation of magnesium phosphate conversion coatings on AZ31 magnesium alloy, Appl. Surf. Sci. 492 (2019) 314–327, https://doi.org/10.1016/J.APSUSC.2019.05.309.

[32] C. Kavitha, T.S.N.N. Sankara Narayanan, K. Ravichandran, I.S. Park, M.H. Lee, Deposition of zinc–zinc phosphate composite coatings on steel by cathodic electrochemical treatment, J. Coat. Technol. Res. 11 (2014) 431–442, https://doi.org/10.1007/s11998-013-9533-z.

[33] L. Herschke, V. Enkelmann, I. Lieberwirth, G. Wegner, The role of hydrogen bonding in the crystal structures of zinc phosphate hydrates, Chem. A Eur. J. 10 (2004) 2795–2803, https://doi.org/10.1002/CHEM.200305693.

[34] A.A. Oskuie, A. Afshar, H. Hasannejad, Effect of current density on DC electrochemical phosphating of stainless steel 316, Surf. Coat. Technol. 205 (2010) 2302–2306, https://doi.org/10.1016/j.surfcoat.2010.09.016.

[35] A. Mehrvarz, Y. Ghazanfar-Ahari, J. Khalil-Allafi, S. Mahdavi, M. Etminanfar, The microstructural features and corrosion behavior of hydroxyapatite/ZnO nanocomposite electrodeposit on NiTi alloy: effect of current density, Ceram. Int. 48 (2022) 2191–2202, https://doi.org/10.1016/j.ceramint.2021.09.311.

[36] S. Chen, W. Liu, Z. Huang, X. Liu, Q. Zhang, X. Lu, The simulation of the electrochemical cathodic Ca–P deposition process, Mater. Sci. Eng. C 29 (2009) 108–114, https://doi.org/10.1016/j.msec.2008.05.016.

[37] G.C. Sosso, J. Chen, S.J. Cox, M. Fitzner, P. Pedevilla, A. Zen, A. Michaelides, Crystal nucleation in liquids: open questions and future challenges in molecular dynamics simulations, Chem. Rev. 116 (2016) 7078–7116, https://doi.org/10.1021/acs.chemrev.5b00744.

[38] D. Gebauer, M. Kellermeier, J.D. Gale, L. Bergström, H. Cölfen, Pre-nucleation clusters as solute precursors in crystallisation, Chem. Soc. Rev. 43 (2014) 2348–2371, https://doi.org/10.1039/C3CS60451A.

[39] J.J. De Yoreo, P.G. Vekilov, Principles of crystal nucleation and growth, Rev. Mineral. Geochem. 54 (2003) 57–93, https://doi.org/10.2113/0540057.

[40] Q. Hu, M.H. Nielsen, C.L. Freeman, L.M. Hamm, J. Tao, J.R.I. Lee, T.Y.J. Han, U. Becker, J.H. Harding, P.M. Dove, J.J. De Yoreo, The thermodynamics of calcite nucleation at organic interfaces: classical vs. non-classical pathways, Faraday Discuss 159 (2012) 509–523, https://doi.org/10.1039/c2fd20124k.

[41] C.L. Freeman, J.H. Harding, The transformation of amorphous calcium carbonate to calcite and classical nucleation theory, J. Cryst. Growth 603 (2023) 126978, https://doi.org/10.1016/J.JCRYSGRO.2022.126978.

[42] X. Lu, Y. Leng, Theoretical analysis of calcium phosphate precipitation in simulated body fluid, Biomaterials 26 (2005) 1097–1108, https://doi.org/10.1016/J.BIOMATERIALS.2004.05.034.

[43] M. Emmanuel, P. Papp, G. Schuszter, Á. Deák, L. Janovák, Á. Tóth, D. Horváth, Nucleation kinetics of lithium phosphate precipitation, CrystEngComm 24 (2022) 4447–4453, https://doi.org/10.1039/D2CE00333C.

[44] S. Jegannathan, T.S.N. Sankara Narayanan, K. Ravichandran, S. Rajeswari, Performance of zinc phosphate coatings obtained by cathodic electrochemical treatment in accelerated corrosion tests, Electrochim. Acta 51 (2005) 247–256, https://doi.org/10.1016/j.electacta.2005.04.020.

[45] F.J.J. Kellner, K. Schütze, C. Kreutz, S. Virtanen, Electrochemical and surface analytical study of the corrosion behavior of mild steel with cathodically produced zinc phosphate coating, Surf. Interface Anal. 41 (2009) 911–917, https://doi.org/10.1002/sia.3118.

[46] H. Liu, Y. Zhang, C. Wang, J.N. Glazer, Z. Shan, N. Liu, Understanding and controlling the nucleation and growth of Zn electrodeposits for aqueous zinc-ion batteries, ACS Appl. Mater. Interfaces 13 (2021) 32930–32936, https://doi.org/10.1021/acsami.1c06131.

[47] M.G. Chu, J. McBreen, G. Adzic, Substrate effects on zinc deposition from zincate solutions: i: deposition on Cu, Au, Cd and Zn, J. Electrochem. Soc. 128 (1981) 2281–2286, https://doi.org/10.1149/1.2127235.

[48] J. McBreen, M.G. Chu, G. Adzic, Substrate effects on zinc deposition from zincate solutions: II: deposition on Pb, Tl, Sn, and In, J. Electrochem. Soc. 128 (1981) 2287–2292, https://doi.org/10.1149/1.2127236.

[49] A. Erbe, P. Schneider, C. Gadiyar, F.U. Renner, Electrochemically triggered nucleation and growth of zinc phosphate on aluminium-silicon-coated steel, Electrochim. Acta 182 (2015) 1132–1139, https://doi.org/10.1016/J.ELECTACTA.2015.09.094.

[50] Z. Xing, Y. Sun, X. Xie, Y. Tang, G. Xu, J. Han, B. Lu, S. Liang, G. Chen, J. Zhou, Zincophilic electrode interphase with appended proton reservoir ability stabilizes Zn metal anodes, Angew. Chemie Int. Ed. 62 (2023) e202215324, https://doi.org/10.1002/ANIE.202215324.

[51] X. Song, L. Bai, C. Wang, D. Wang, K. Xu, J. Dong, Y. Li, Q. Shen, J. Yang, Synergistic cooperation of Zn(002) texture and amorphous zinc phosphate for dendrite-free Zn Anodes, ACS Nano 17 (2023) 15113–15124, https://doi.org/10.1021/acsnano.3c04343.

[52] D. Barnes, S. Johnson, R. Snell, S. Best, Using scratch testing to measure the adhesion strength of calcium phosphate coatings applied to poly(carbonate urethane) substrates, J. Mech. Behav. Biomed. Mater. 6 (2012) 128–138, https://doi.org/10.1016/J.JMBBM.2011.10.010.

[53] J. Wang, P. Layrolle, M. Stigter, K. De Groot, Biomimetic and electrolytic calcium phosphate coatings on titanium alloy: physicochemical characteristics and cell attachment, Biomaterials 25 (2004) 583–592, https://doi.org/10.1016/S0142-9612(03)00559-3.

[54] I.Y. Ortiz, A. Raybolt dos Santos, A.M. Costa, E. Mavropoulos, M.N. Tanaka, M.H. Prado da Silva, S. de Souza Camargo, *In vitro* assessment of zinc apatite coatings on titanium surfaces, Ceram. Int. 42 (2016) 15502–15510, https://doi.org/10.1016/J.CERAMINT.2016.06.203.

[55] D. Ernens, M.B. de Rooij, H.R. Pasaribu, E.J. van Riet, W.M. van Haaften, D.J. Schipper, Mechanical characterization and single asperity scratch behaviour of dry zinc and manganese phosphate coatings, Tribol. Int. 118 (2018) 474–483, https://doi.org/10.1016/j.triboint.2017.04.034.

[56] D. Ernens, G. Langedijk, P. Smit, M.B. de Rooij, H.R. Pasaribu, D.J. Schipper, Characterization of the adsorption mechanism of manganese phosphate conversion coating derived tribofilms, Tribol. Lett. 66 (2018) 131, https://doi.org/10.1007/s11249-018-1082-2.

[57] L. Zang, Q. Zhong, Y. Chen, W. Hou, B. Zhao, Y. Wu, Effect of coating thickness on tribological properties of manganese phosphate conversion coating in different motion conditions, Tribol. Int. 176 (2022) 107894, https://doi.org/10.1016/J.TRIBOINT.2022.107894.

[58] K. Abdalla, R. Azmi, A. Azizan, The effect of ph on zinc phosphate coating morphology and its corrosion resistance on mild steel, Adv. Mater. Res. 626 (2012) 569–574, https://doi.org/10.4028/www.scientific.net/AMR.626.569.

[59] Z. Panossian, L. Mariaca, M. Morcillo, S. Flores, J. Rocha, J.J. Peña, F. Herrera, F. Corvo, M. Sanchez, O.T. Rincon, G. Pridybailo, J. Simancas, Steel cathodic protection afforded by zinc, aluminium and zinc/aluminium alloy coatings in the atmosphere, Surf. Coat. Technol. 190 (2005) 244–248, https://doi.org/10.1016/J.SURFCOAT.2004.04.023.

[60] F. Thébault, B. Vuillemin, R. Oltra, C. Allely, K. Ogle, Protective mechanisms occurring on zinc coated steel cut-edges in immersion conditions, Electrochim. Acta 56 (2011) 8347–8357, https://doi.org/10.1016/J.ELECTACTA.2011.07.016.

[61] E. McCafferty, Validation of corrosion rates measured by the Tafel extrapolation method, Corros. Sci. 47 (2005) 3202–3215, https://doi.org/10.1016/j.corsci.2005.05.046.

[62] F. Mansfeld, M.W. Kendig, S. Tsai, Evaluation of corrosion behavior of coated metals with AC impedance measurements, Corrosion 38 (1982) 478–485, https://doi.org/10.5006/1.3577363.

[63] B. Hirschorn, M.E. Orazem, B. Tribollet, V. Vivier, I. Frateur, M. Musiani, Determination of effective capacitance and film thickness from constant-phase-element parameters, Electrochim. Acta 55 (2010) 6218–6227, https://doi.org/10.1016/J.ELECTACTA.2009.10.065.

[64] D.M. Bastidas, Interpretation of impedance data for porous electrodes and diffusion processes, Corrosion 63 (2007) 515–521, https://doi.org/10.5006/1.3278402.

[65] A. Lasia, Impedance of porous electrodes, J. Electroanal. Chem. 397 (1995) 27–33, https://doi.org/10.1016/0022-0728(95)04177-5.

[66] S. Silva-Fernández, B. Díaz, R. Figueroa, X.R. Nóvoa, C. Pérez, A comprehensive structural and electrochemical study on the performance of Mn-phosphate layers, Surf. Coat. Technol. 476 (2024) 130260, https://doi.org/10.1016/J.SURFCOAT.2023.130260.

[67] X. He, J. Wu, Y. Chen, L. Zhang, X. Sheng, A trace amount of MXene@PDA nanosheets for low-temperature zinc phosphating coatings with superb corrosion resistance, Appl. Surf. Sci. 603 (2022) 154455, https://doi.org/10.1016/j.apsusc.2022.154455.

[68] Y. Tian, H. Huang, H. Wang, Y. Xie, X. Sheng, L. Zhong, X. Zhang, Accelerated formation of zinc phosphate coatings with enhanced corrosion resistance on carbon steel by introducing α-zirconium phosphate, J. Alloys Compd. 831 (2020) 154906, https://doi.org/10.1016/j.jallcom.2020.154906.

[69] M. Mahdavian, M.M. Attar, Another approach in analysis of paint coatings with EIS measurement: phase angle at high frequencies, Corros. Sci. 48 (2006) 4152–4157, https://doi.org/10.1016/J.CORSCI.2006.03.012.

[70] Y. Xie, M. Chen, D. Xie, L. Zhong, X. Zhang, A fast, low temperature zinc phosphate coating on steel accelerated by graphene oxide, Corros. Sci. 128 (2017) 1–8, https://doi.org/10.1016/J.CORSCI.2017.08.033.

[71] R. Amini, A.A. Sarabi, The corrosion properties of phosphate coating on AZ31 magnesium alloy: the effect of sodium dodecyl sulfate (SDS) as an eco-friendly accelerating agent, Appl. Surf. Sci. 257 (2011) 7134–7139, https://doi.org/10.1016/J.APSUSC.2011.03.072.